Applied Thermal Engineering 151 (2019) 495–505

Contents lists available at ScienceDirect

Applied Thermal Engineering

journal homepage: www.elsevier.com/locate/apthermeng

Research Paper

A two-dimensional mathematical model for vanadium redox flow battery stacks incorporating nonuniform electrolyte distribution in the flow frame

B.W. Zhang[a], Y. Lei[a], B.F. Bai[a], A. Xu[b], T.S. Zhao[b,*]

[a] State Key Laboratory of Multiphase Flow in Power Engineering, Xi'an Jiaotong University, Xi'an 710049, China
[b] HKUST Energy Institute, Department of Mechanical and Aerospace Engineering, The Hong Kong University of Science and Technology, Hong Kong, China

HIGHLIGHTS

- A two-dimensional mathematical model for the VRFB stack is reported.
- Electrolyte distribution is described via flow network equivalence method.
- Reversible and irreversible heat sources in stack are determined.
- Nonuniform electrolyte distribution dramatically influences discharge capacity.

ARTICLE INFO

Keywords:
Vanadium redox flow battery stack
Battery thermal management
Two-dimensional thermal model
Nonuniform electrolyte distribution

ABSTRACT

Lumped models have been widely adopted to predict the performance of the vanadium redox flow battery (VFRB) stack, which mainly due to its simplicity in modeling transient behaviors during operation cycles. However, average transport and electrochemical properties in previous lumped models make it impossible to obtain the information of electrolyte distributions in stacks. To address this issue, in this work, we report a two-dimensional mathematical model for a VRFB stack considering the effect of nonuniform electrolyte distributions in the flow frame via a flow network equivalence method. With this new model, battery performance and its temperature at different operating conditions are determined accurately. It is demonstrated that (i) temperature fluctuations of the stack reach up to 10 K at different current densities and flow rates; (ii) 25% blockage in the middle cell can lead to the capacity reduction by up to 80%.

1. Introduction

Redox flow batteries are promising large-scale energy storage devices to tackle the issue of intermittent renewable power supply [1]. Compared with traditional batteries in which active substances are contained inside the electrodes, redox flow batteries conserving active substances in externally stored electrolyte, resulting in decoupled power and capacity. This charming feature dramatically expands the scalability of flow battery, making them attractive energy storage systems to meet various demands. Especially, the VRFBs eliminate the crossover contamination via utilization of vanadium ions in both positive and negative electrolytes, thus exhibiting long cycle life. Despite the fruitful achievements in the VRFB, some technique barriers still restrict its commercialization.

Previous studies have revealed that high-efficient modular stack, electrolyte with high stability and concentration and reliable thermal management are essential for the long-term operation of large-scale VRFB system. However, at considerably high temperature, pentavalent vanadyl ions cycling in batteries tend to become unstable and easily precipitate in concentrated electrolyte. Bivalent vanadium ions, trivalent vanadium ion and tetravalent vanadyl ions form insoluble substances at low temperature [2]. During the cyclic operation of VRFB, the variation of electrolyte temperature is determined by the heat generation in stack and heat dissipation into the ambience. For the industrial-scale VRFB system, electrolyte temperature varies within a wide range, exceeding the temperature limits easily. On occasion that the VRFB system is operated at an inappropriate temperature, vanadium ions tend to precipitate in electrolyte. The precipitation in electrolyte degrades the electrochemical reaction rate results from the decrease of vanadium ions concentration. Once large amount of precipitation forms in electrolyte and blocks the void space in the porous electrodes, energy efficiency of the battery reduces dramatically. In severe cases, it even leads to the breakdown of VRFB system. All these deficiencies require a rational and efficient thermal

* Corresponding author.
E-mail address: metzhao@ust.hk (T.S. Zhao).

https://doi.org/10.1016/j.applthermaleng.2019.02.037
Received 23 December 2018; Received in revised form 23 January 2019; Accepted 9 February 2019
Available online 11 February 2019
1359-4311/

Nomenclature

A	area, m^2
a	specific surface area, m^{-1}
C_p	specific heat capacity, $J{\cdot}kg^{-1}{\cdot}K^{-1}$
c	concentration, $mol{\cdot}m^{-3}$
D	diffusion coefficient, $m^2{\cdot}s^{-1}$
d_f	fiber diameter, m
E	potential, V
F	Faraday constant, $C{\cdot}mol^{-1}$
p	pressure, Pa
Q	heat source, W
q	power density of heat source, $W{\cdot}m^{-3}$
R	gas constant, $J{\cdot}mol^{-1}{\cdot}K^{-3}$
S	mass source, $mol{\cdot}m^{-3}$
T	temperature, K
V	electrolyte volume, m^3
v	electrolyte flow velocity, $m{\cdot}s^{-1}$
z	valence

Greek

ε	porosity
η	over-potential, V
λ	thermal conductivity, $W{\cdot}m^{-1}{\cdot}K^{-1}$
μ	dynamic viscosity, Pa·s
ρ	density, $kg{\cdot}m^{-3}$
σ	conductivity, $S{\cdot}m^{-1}$
ϕ	potential, V
ω	electrolyte flow rate, $m^3{\cdot}s^{-1}$

Superscripts and subscripts

i = 2, 3, 4, 5, H	vanadium ions (V^{2+}, V^{3+}, VO^{2+}, VO_2^{+}) and hydrogen ion
e	electrolyte
s	porous graphite electrode
res	electrolyte reservoir
m	ion exchange membrane
bp	bipolar plate
ch	channel in flow frame
ma	manifold in flow frame
in	inlet
out	outlet
inner	inner surface
outer	outer surface
interface	interface of electrode and membrane

management system and accurate prediction of battery temperature so that we can control it within an appropriate range to achieve long-term utilization of the VRFB.

Based on the systematic analysis, mathematical models have been aiding the development of the VRFB system. In previous models, the momentum, mass, charge, energy conservation equations together with electrochemical kinetics are coupled to describe the transport processes in the VRFB. Since a lumped model that concerns mass transport and electrochemical reactions proposed by Li et al. [3], numerous studies on modeling the VRFB in single cell have been reported [4–18]. Shah and coworkers established a two-dimensional model describing the fluid flow, species transport, and electrochemical reactions in porous electrodes [4]. On this basis, they developed a non-isothermal model to investigate the temperature and heat generation in VRFB [5]. In addition, models incorporating the effects of vanadium crossover through membrane and influence of porous electrode properties were proposed [6–13]. Wei et al. reported the control-oriented models for the he management of VRFBs [14–16]. These models are utilized to monitor the online monitoring of capacity loss and state of charge in real time. The online adaption models capture the battery behavior accurately. With more realistic conditions considered, several three-dimensional models were also developed to study the effect of flow field structure and temperature on battery performance [17,18].

In addition to the models describing transport processes and electrochemical reactions in single cell, dynamic models stressed on the cell organization instead of transport and distribution details have also been developed [19–23]. The influence of various key factors on battery stack performance and temperature were investigated during operation cycles [19,20]. Moreover, stack models concerning flow and connection patterns in stack of the VRFB system were reported [21–23]. In the lump models for VRFB system with stack involved, average transport and electrochemical properties are applied. Despite the relatively low computation burden, distribution details of electrochemical reactions and mass transport cannot be fully revealed. Considering the significant effect on mass, heat transport and electrochemical reactions, non-uniformity of electrolyte distribution needs to be investigated comprehensively. Moreover, the uniformity of electrolyte distribution among cells requires the proper design of channels and manifolds in flow frame. To meet the requirements, the structure of flow frame is usually designed in high tortuosity and complexation, increasing the computation burden consequently. Herein, more efficient model which involves the transport details and reduces the model complexation and computation burden is urgently in need.

In this work, we report a two-dimensional mathematical model for the VRFB stack. With the utilization of a flow network equivalence method, the effect of nonuniform electrolyte distributions in the flow frame is considered. With this new model, heat source and temperature during operation cycles were investigated. The effects of operating conditions, such as current densities and flow rates are simulated. Conditions that stack was partially blocked by vanadium precipitation and the effect on battery performance were also studied, as well as the determination of the electrolyte distribution and discharge capacity. In Section 2, a mathematical model describing the transport phenomena in VRFB system is presented. Then, the simulation results are presented and discussed in Section 3, followed by the conclusions.

2. Mathematical model

The schematic diagram of a VRFB system are depicted in Fig. 1. For a practical stacked battery system, ion exchange membranes separate the positive and negative electrodes in each cell, which barriers electrons and vanadium ions. The inner circuit through membrane is conducted by hydrogen ions in electrolytes. The conductive plates of each cell connect in series, forming the packed stack of VRFB. Electrolytes are pumped between cells stack and reservoirs in operation. Considering the relatively slow changes in ion concentration and flow conditions, a series of simplifications and assumptions are introduced: local thermal equilibrium and dilute solution theory are applied; electrolyte mixes immediately and uniformly distribute in reservoirs; volume of electrolyte is constant; side reactions such as the oxygen and hydrogen evolution are ignored.

2.1. Modeling of electrolyte flow in the flow frame

In the VRFB, the electrolyte containing active substances is pumped cyclically between cells stack and reservoirs, supplying sufficient reactants for electrochemical reactions in porous electrodes and removing the resultants and redundant reactants. This process induces the power

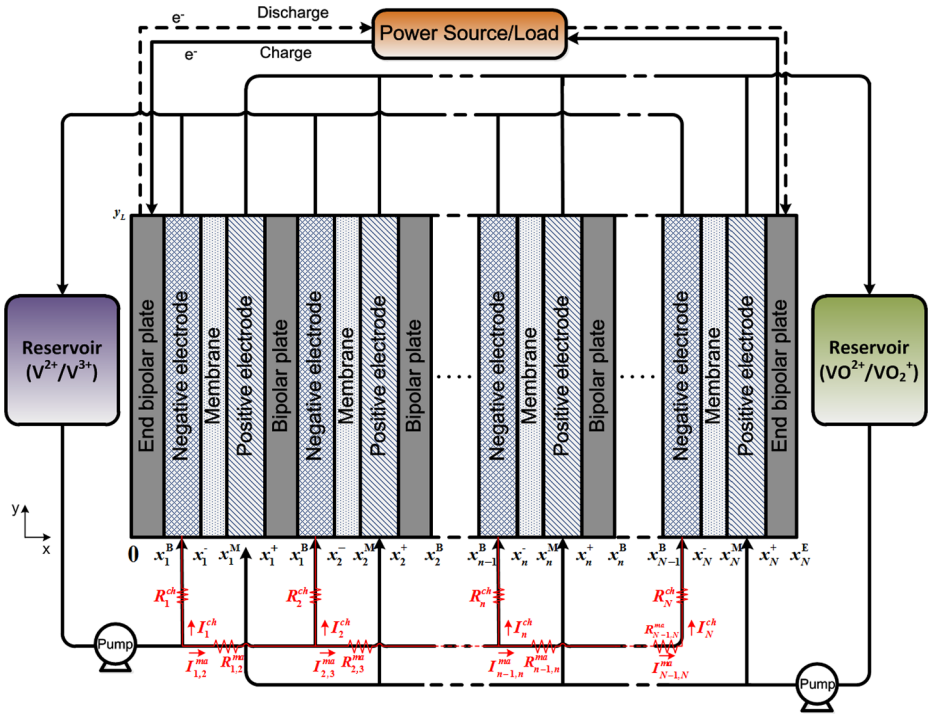

Fig. 1. Schematic diagram of vanadium redox flow battery system.

loss associated with pressure drop in VRFB system. Electrolyte flow in channels and manifolds of flow frame is treated as pipe flow. According to the description of pipe flow in Chapter 8 of literature [24], the pressure drop of electrolyte flow in pipes can be expressed as:

$$\Delta p = \frac{1}{2}\rho\frac{f_d L}{D_h}v^2 \tag{1}$$

where v denotes the electrolyte flow velocity, which is calculated according to the electrolyte flow rates in flow frame: $v = \omega/A$. ρ denotes the electrolyte density, L and A denote the length and cross section area of channels and manifolds. ω denotes the electrolyte flow rate. D_h is hydrolytic diameter of rectangular channels or circular manifolds [24], which is expressed as:

$$D_h = \begin{cases} \frac{2L_h L_w}{L_h + L_w}, & \text{rectangular} \\ D_{ma}, & \text{circular} \end{cases} \tag{2}$$

where L_h and L_w denote the height and width of channels, while D_{ma} denotes the manifold diameter in the electrolyte flow frame. Moreover, Darcy fraction factors are calculated by [24]:

$$f_d = \begin{cases} \frac{55.5 + 40.9 \times 0.03^{L_h/L_w}}{\mathrm{Re}}, & \text{rectangular} \\ \frac{64}{\mathrm{Re}}, & \text{circular} \end{cases} \tag{3}$$

where *Re* denotes the Reynolds number in channels and manifolds. The electrolyte is pumped from the reservoirs and then forced flowing through the flow frame and porous electrodes. In the flow frame, the electrolyte is distributed through channels and manifolds and the electrolyte flow is considered as pipe flow. Along with direction from (n-1)th cell to the nth cell in flow frame, the pressure drop in the (n-1)th channel, (n-1)th manifold and nth channel are expressed as: $-\Delta p_{n-1}^{ch}$, Δp_{n-1}^{ma} and Δp_n^{ch} respectively. The sum of these terms equals the pressure drop between the adjacent cells in stack, which is expressed as:

$$-\Delta p_{n-1}^{ch} + \Delta p_n^{ch} + \Delta p_{n-1}^{ma} = p_{n-1} - p_n, \qquad n = 2, \quad 3, \quad \ldots, \quad N \tag{4}$$

where *ch* and *ma* denote the channels and manifolds, respectively.

Combined the pressures drop in pipe flow as shown in Eq. (1) with the Eq. (4), the equations for pressure drop between adjacent cells in a stack composed of N cells can be drawn [24]:

$$-\frac{f_d}{2}\frac{L_{ch}}{D_h}\rho\left(\frac{\omega_{n-1}^{ch}}{A^{ch}}\right)^2 + \frac{f_d}{2}\frac{L_{ch}}{D_h}\rho\left(\frac{\omega_n^{ch}}{A^{ch}}\right)^2 + \frac{f_d}{2}\frac{L_{ma}}{D_h}\rho\left(\frac{\omega_{n-1}^{ma}}{A^{ma}}\right)^2 = p_{n-1} - p_n, \qquad n = 2, \quad 3, \quad \ldots, \quad N \tag{5}$$

There are no source terms of electrolyte mass transport in the flow frame. According to the mass conservation, the electrolyte flow rates in channels and manifolds are calculated as:

$$\begin{cases} \omega_{n-1,n}^{ma} - \omega_{n,n+1}^{ma} - \omega_n^{ch} = 0, & n = 2, \quad 3, \quad \ldots, \quad N-1 \\ \omega_{1,2}^{ma} + \omega_1^{ch} = \omega, & n = 1 \\ \omega_{N-1,N}^{ma} - \omega_N^{ch} = 0, & n = N \end{cases} \tag{6}$$

When electrolyte is pumped into the stack, it flows through the manifolds and channels carved in flow frame. With appropriate design of flow frame, the electrolyte can not only flow uniformly in every single cell, but also be distributed evenly among each part of porous electrode. The conductive electrolyte fills the flow frame and porous electrodes, connecting every cell in the stack. Electrolyte circuit in flow frame was analogically simulated. Considering the similarity of design at inlet and outlet of both positive and negative flow frames, only part of the model at negative inlet is depicted in Fig. 1. R_n^c and $R_{n-1,n}^m$ refer to electrolyte resistances in channels and manifolds, respectively. They are calculated from the electrolyte conductivity and flow frame specifications as [23]:

$$\begin{aligned} R_n^{ch} &= \frac{L^{ch}}{\sigma_e A^{ch}} \\ R_n^{ma} &= \frac{L^{ma}}{\sigma_e A^{ma}} \end{aligned} \tag{7}$$

The electrolyte conductivity varies along with the state of charge (SOC) [25]:

$$\sigma_e = \begin{cases} 17.69 + 7.50 \times \mathrm{SOC}^- \ \text{(Negative electrolyte)} \\ 27.67 + 13.36 \times \mathrm{SOC}^+ \ \text{(Positive electrolyte)} \end{cases} \tag{8}$$

The SOC is derived from concentrations of vanadium ions in negative and positive electrolyte:

$$\begin{aligned} \mathrm{SOC}^{-} &= \frac{c_2}{c_2 + c_3} \\ \mathrm{SOC}^{+} &= \frac{c_5}{c_4 + c_5} \end{aligned} \tag{9}$$

where c_2, c_3, c_4, c_5 refers to the vanadium ion concentrations of V^{2+}, V^{3+}, VO^{2+}, $VO_2{}^{+}$, respectively. At the inlet and outlet of porous electrodes, Kirchhoff's law is applied to calculate inward currents as [23]:

$$\begin{cases} -I_{n-1}^{ch} R_{n-1}^{ch} + I_n^{ch} R_n^{ch} + I_{n-1,n}^{ma} R_{n-1,n}^{ma} = \bar{\phi}_{n-1} - \bar{\phi}_n, & n = 2, 3, \ldots, N \\ I_{n-1,n}^{ma} - I_{n,n+1}^{ma} - I_n^{ch} = 0, & n = 2, 3, \ldots, N-1 \\ I_{1,2}^{ma} + I_1^{ch} = 0, & n = 1 \\ I_{N-1,N}^{ma} - I_N^{ch} = 0, & n = N \end{cases} \tag{10}$$

where average potentials $\bar{\phi}_n$ at inlet and outlet of every half-cell can be expressed as $\int \phi_n \mathrm{d}l / L_d$, and L_d is the width of porous electrode at inlet and outlet. The SOC in different cells varies with the change of the vanadium ion concentrations, resulting in the variation of electrolyte resistances. Therefore, electrolyte current I_n^{ch} at inlets and outlets boundaries should be updated iteratively along with the calculation in porous electrodes.

2.2. Modeling of charge and mass transport in ion exchange membrane

In ion exchange membranes, there is no reaction occurring. Thus, the electrical potential drop across membranes is described with Ohm' law [8]:

$$\Delta\phi^m = -i^m d_m / \sigma^{m,eff} \tag{11}$$

where i^m is current density in membrane, and d_m is membrane thickness. $\sigma^{m,eff}$ denotes the effective conductivity of ion exchange membrane and is expressed as [8]:

$$\sigma^{m,eff} = -(F^2/RT) z_f^2 c_f D_{\mathrm{H}^+}^m \tag{12}$$

where z_f and c_f denote charge and concentration of fixed sulfonic acid group in membrane respectively. F is Faraday constant, R is gas constant, T is temperature in stack. $D_{\mathrm{H}^+}^m$ is diffusion coefficient of hydrogen ion in membrane.

At the interfaces of ion exchange membrane and electrolyte in porous electrodes, the selective permeability of membranes leads to the potential difference across the interfaces, namely Donnan potential. In each single cell, Donnan potentials at negative and positive side of interfaces are expressed as [10]:

$$\begin{aligned} \phi_{neg}^D &= \phi_{neg}^{e,interface} - \phi_{neg}^{m,interface} = \frac{RT}{F} \ln\left(\frac{c_{\mathrm{H}^+,neg}^{e,interface}}{c_{\mathrm{H}^+,neg}^{m,interface}} \right) \\ \phi_{pos}^D &= \phi_{pos}^{e,interface} - \phi_{pos}^{m,interface} = \frac{RT}{F} \ln\left(\frac{c_{\mathrm{H}^+,pos}^{e,interface}}{c_{\mathrm{H}^+,pos}^{m,interface}} \right) \end{aligned} \tag{13}$$

where the superscript *interface* denotes the interface between membrane and porous electrode. Superscript e and m denote the concentrations of hydrogen ions in electrolytes and membranes, respectively.

Mass transfer in membranes is assumed to be quasi-steady due to the relatively slow variation of ions concentration. According to the Nernst-Planck equation applied in literature [8], the conservation equations for transport of vanadium ions in membrane can be simplified as:

$$-D_i^m \frac{\mathrm{d}(c_i^m)^2}{\mathrm{d}^2 x} + \left(\frac{z_i D_i^m F i^m}{RT\sigma^{m,eff}} + v^m \right) \frac{\mathrm{d}c_i^m}{\mathrm{d}x} = 0 \tag{14}$$

where i (2, 3, 4, 5) denotes the vanadium ions, D_i^m denotes effective diffusion coefficient of vanadium ions in membrane, z_i denotes the valence of vanadium ions. The electrolyte velocity in membrane is described by [4]:

$$v^m = -\frac{\kappa_p}{\mu} \nabla p - \frac{\kappa_\phi}{\mu} c_f F \nabla \phi^m \tag{15}$$

where κ_p and κ_ϕ denote the hydraulic and electro-kinetic permeability respectively. Parameters of charge and mass transport in membrane from the literature [26] are listed in Table 1.

To be expressed clearly, the expression $\frac{z_i D_i^{m,\mathrm{eff}} F i^m}{RT\sigma^{m,eff}} + v^m$ is defined as M_i. Concentrations of vanadium ions in membrane are derived from Eq. (14) combining with boundary conditions of Eqs. (43) and (45). Herein, the concentration of V^{2+}, V^{3+} in membrane are expressed as:

$$c_i^m = c_i^{interface} \frac{\exp\left(\frac{-M_i (d_m - x)}{D_i^{m,\mathrm{eff}}} \right) - 1}{\exp\left(\frac{-M_i d_m}{D_i^{m,\mathrm{eff}}} \right) - 1} \tag{16}$$

Concentration of VO^{2+}, $VO_2{}^{+}$ in membrane are:

$$c_i^m = c_i^{interface} \frac{\exp\left(\frac{M_i x}{D_i^{m,\mathrm{eff}}} \right) - 1}{\exp\left(\frac{M_i d_m}{D_i^{m,\mathrm{eff}}} \right) - 1} \tag{17}$$

where $c_i^{interface}$ (i = 2, 3, 4, 5) denotes the vanadium concentration at the interface of membrane and porous electrodes, x denotes the location in membrane away from the negative interface.

2.3. Modeling of heat transfer in VRFB system

The temperature changes during operation are determined by the heat production and heat dissipation in each component of the VRFB system. Heat sources in system include the Joule heat associated with the Ohmic resistances, activation heat losses, reversible electrochemical reaction heat and chemical reaction heat losses caused by crossover of vanadium ions through membranes in stack, and the fraction heat losses along with the circular flowing electrolyte in system. Among them, the Joule heat is produced when current conducted in membranes, bipolar plates, porous electrodes and electrolytes. Heat transport due to electrolyte flows in the stack can be described as [5]:

$$\begin{aligned} (\rho \bar{C}_\mathrm{p})_{stack} V_{stack} \frac{\mathrm{d}T_{stack}}{dt} + (\rho C_\mathrm{p})_e ((\omega_{out}^- + \omega_{out}^+) T_{stack} - \omega_{in}^- T_{in}^- - \omega_{in}^+ T_{in}^+) \\ + U_{stack} A_{stack} (T_{stack} - T_a) = Q_{stack} \end{aligned} \tag{18}$$

where $(\rho \bar{C}_\mathrm{p})_{stack}$ denotes the average thermal capacitance in stack, T_a denotes the ambient temperature. V, A, T are volume, surface area, and

Table 1
Parameters of charge and mass transport in membrane.

Parameter	Value [26]
Diffusion coefficient of V^{2+} in membrane, D_2^m	$8.768 \times 10^{-12}\ \mathrm{m^2 \cdot s^{-1}}$
Diffusion coefficient of V^{3+} in membrane, D_3^m	$3.222 \times 10^{-11}\ \mathrm{m^2 \cdot s^{-1}}$
Diffusion coefficient of VO^{2+} in membrane, D_4^m	$6.825 \times 10^{-12}\ \mathrm{m^2 \cdot s^{-1}}$
Diffusion coefficient of VO_2^+ in membrane, D_5^m	$5.897 \times 10^{-12}\ \mathrm{m^2 \cdot s^{-1}}$
Hydrogen diffusion coefficient in membrane, $D_{H^+}^m$	$3.35 \times 10^{-10}\ \mathrm{m^2 \cdot s^{-1}}$
Membrane thickness, d_m	$1.27 \times 10^{-4}\ \mathrm{m}$
Concentration of fixed charge in membrane, c_f	$1200\ \mathrm{mol \cdot m^{-3}}$
Charge of fixed site, z_f	-1
Hydraulic permeability in membrane, κ_p	$1.58 \times 18\ \mathrm{m^2}$
Electro-kinetic permeability in membrane, κ_ϕ	$1.13 \times 20\ \mathrm{m^2}$

temperature, respectively. The subscripts *in, out* denote electrolyte flowing in and out. Thermal parameters in stack are listed in Table 2 and heat source densities in electrodes are listed in Table 3.

Table 2
Thermal parameters in stack.

Parameter	Value [5]
Thermal capacitance of solid matrix, $(\rho C_p)_s$	3.33×10^5 J·m^{-3}·K^{-1}
Thermal capacitance of electrolyte, $(\rho C_p)_e$	4.18×10^6 J·m^{-3}·K^{-1}
Thermal capacitance of bipolar plate, $(\rho C_p)_{bp}$	4.03×10^6 J·m^{-3}·K^{-1}
Thermal capacitance of membrane, $(\rho C_p)_m$	2.18×10^6 J·m^{-3}·K^{-1}
Entropy change in negative reaction, ΔS_{neg}	100 J·mol^{-1}·K^{-1}
Entropy change in positive reaction, ΔS_{pos}	21.7 J·mol^{-1}·K^{-1}
Thermal conductivity of electrolyte, λ_e	0.67 W·m^{-1}·K^{-1}
Thermal conductivity of electrode, λ_s	0.15 W·m^{-1}·K^{-1}
Thermal conductivity of air, λ_{air}	0.0257 W·m^{-1}·K^{-1}

Table 3
Heat source densities in electrodes.

Parameter	Negative side	Positive side
q_{ohmic}	$\sigma_s^{eff}\lvert\nabla\phi_s\rvert^2 + \sigma_e^{eff}\lvert\nabla\phi_e\rvert^2$	$\sigma_s^{eff}\lvert\nabla\phi_s\rvert^2 + \sigma_e^{eff}\lvert\nabla\phi_e\rvert^2$
$q_{activation}$	$\eta_{neg} i_{neg}$	$\eta_{pos} i_{pos}$
$q_{electrochemical\ reaction}$	$-\Delta S_{neg} Ti_{neg}/F$	$\Delta S_{pos} Ti_{pos}/F$

Heat transfer coefficients for planar and cylindrical walls are described as:

$$U_{planar} = \frac{1}{1/h_{inner} + 1/h_{outer} + \delta/\lambda}$$
$$U_{cylindrical} = \frac{1}{1/h_{inner} + (D_{res}/(D_{res}+2\delta))(1/h_{outer}) + (D_{res}/2\lambda)\ln((D_{res}+2\delta)/D_{res})} \quad (19)$$

where δ denotes wall thickness, D_{res} denotes the diameter of cylindrical surface, and λ denotes thermal conductivity of walls. Convection heat transfer coefficient for surfaces of stack, pips and reservoirs is described as $h = Nu_f \lambda_f / L$, where Nu_f denotes the Nusselt number, λ_f denotes the thermal conductivity of fluid, and L denotes the characteristic length.

Heat transfer between pipes and ambience at negative side can be described as:

$$(\rho C_p)_e V_{in}^- \frac{dT_{in}^-}{dt} + (\rho C_p)_e \omega_{in}^- (T_{in}^- - T_{res}^-) + U_{in}^- A_{in}^- (T_{in}^- - T_a) = Q_{pipe\ fraction,in}^-$$
$$(\rho C_p)_e V_{out}^- \frac{dT_{out}^-}{dt} + (\rho C_p)_e \omega_{out}^- (T_{out}^- - T_{stack}) + U_{out}^- A_{out}^- (T_{out}^- - T_a) = Q_{pipe\ fraction,out}^- \quad (20)$$

Meanwhile, heat transfer between electrolyte reservoirs and ambience at negative side can be described as:

$$(\rho C_p)_e V_{res}^- \frac{dT_{res}^-}{dt} + (\rho C_p)_e (\omega_{in}^- T_{res}^- - \omega_{out}^- T_{out}^-) + U_{res}^- A_{res}^- (T_{res}^- - T_a) = 0 \quad (21)$$

Heat transfer between pipes and ambience at positive side is described as:

$$(\rho C_p)_e V_{in}^+ \frac{dT_{in}^+}{dt} + (\rho C_p)_e \omega_{in}^+ (T_{in}^+ - T_{res}^+) + U_{in}^+ A_{in}^+ (T_{in}^+ - T_a) = Q_{pipe\ fraction,in}^+$$
$$(\rho C_p)_e V_{out}^+ \frac{dT_{out}^+}{dt} + (\rho C_p)_e \omega_{out}^+ (T_{out}^+ - T_{stack}) + U_{out}^+ A_{out}^+ (T_{out}^+ - T_a) = Q_{pipe\ fraction,out}^+ \quad (22)$$

Heat transfer between electrolyte reservoirs and ambience at negative side is described as:

$$(\rho C_p)_e V_{res}^+ \frac{dT_{res}^+}{dt} + (\rho C_p)_e (\omega_{in}^+ T_{res}^+ - \omega_{out}^+ T_{out}^+) + U_{res}^+ A_{res}^+ (T_{res}^+ - T_a) = 0 \quad (23)$$

Heat sources in VRFB system except the electrode are listed in Table 4.

Table 4
Heat sources in battery system except electrodes.

Parameter	Equation
$Q_{membrane}$	$\int \frac{(i_l^m)^2}{\sigma^{m,\mathrm{eff}}} L_m L_w dy$
$Q_{bipolar\ plate}$	$\int \frac{(i^{bp})^2}{\sigma^{bp}} L_{bp} L_w dy$
$Q_{shunt\ current}$	$\sum_n ((I_n^{ch})^2 R_n^{ch} + (I_n^{ma})^2 R_n^{ma})$
$Q_{crossover}$	$\sum_i (\int L_w \lvert N_i^m \rvert \Delta H_i dy)$
$Q_{stack\ fraction}$	$(\omega_{in}^- p_{in}^- - \omega_{out}^- p_{out}^-) + (\omega_{in}^+ p_{in}^+ - \omega_{out}^+ p_{out}^+)$
$Q_{pipe\ fraction}$	$-\Delta p \omega_{pipe}$

2.4. Modeling of transport processes and reaction kinetics in porous electrode

Mass transport and electrochemical reactions in porous electrodes are described through a two-dimensional coupled model. According to Darcy's law, momentum conservation of electrolytes can be described as [8]:

$$\frac{\mu}{K}\vec{v} = -\nabla p \quad (24)$$

where μ denotes the electrolyte viscosity. K is the permeability of porous electrode, which is described by Carman-Kozeny equation [27]:

$$K = \frac{d_{fiber}^2 \varepsilon^3}{16 K_{ck}(1-\varepsilon)^2} \quad (25)$$

where d_{fiber}, ε and K_{ck} are the mean fiber diameter, porosity and Carman-Kozeny constant of the porous electrodes, respectively.

Mass conservations of vanadium and hydrogen ions in electrolyte flowing through the porous electrodes are described as follows according to the Nernst-Planck equations [8]:

$$\frac{\partial}{\partial t}(\varepsilon c_i) + \nabla\cdot\left(-D_i^{\mathrm{eff}}\nabla c_i - \frac{z_i c_i D_i^{\mathrm{eff}}}{RT} F \nabla\phi_e + \vec{v} c_i\right) = -S_i \quad (26)$$

where effective diffusion coefficients for species i are expressed as $D_i^{\mathrm{eff}} = \varepsilon^{1.5} D_i$ according to Bruggeman correction. ϕ_e is the electric potential in electrolyte. The source terms S_i of vanadium ions are i_{neg}/F, $-i_{neg}/F$, 0 for V^{2+}, V^{3+}, H^+ in negative electrolyte and i_{pos}/F, $-i_{pos}/F$, $-2i_{pos}/F$ for VO^{2+}, VO_2^+, H^+ in positive electrolyte. i_{neg} and i_{pos} denote the local current sources in negative and positive electrodes respectively. Parameters of charge and mass transport in porous electrode are listed in Table 5.

Charge transfer in negative electrodes is descried by [8]:

$$\nabla\vec{i_s} = -\sigma_s^{eff}\nabla^2\phi_s = i_{neg}$$
$$\nabla\vec{i_e} = -\sigma_e^{eff}\nabla^2\phi_e = -i_{neg} \quad (27)$$

where σ^{eff} denotes the effective conductivity, ϕ denotes electric potential, subscripts *s, e* denote the electrode and electrolyte respectively. Similar equations can be derived for charge transport in positive electrode.

Electrochemical kinetics in porous electrodes is described according to the Butler-Volmer equation [8]. Current sources in porous electrode are described as:

Table 5
Parameters of charge and mass transport in porous electrode.

Parameter	Value [5]
Negative temperature derivative potential, $\frac{dE^0_{neg}}{dT}$	1.5×10^{-3} V K^{-1}
Positive Temperature derivative potential, $\frac{dE^0_{pos}}{dT}$	-9.0×10^{-4} V K^{-1}
Negative electrochemical reaction rate constant, k^{ref}_{neg}	1.7×10^{-7} m·s^{-1}
Positive electrochemical reaction rate constant, k^{ref}_{pos}	6.8×10^{-7} m·s^{-1}
Diffusion coefficient of V^{2+}, D_2	2.4×10^{-10} m^2·s^{-1}
Diffusion coefficient of V^{3+}, D_3	2.4×10^{-10} m^2·s^{-1}
Diffusion coefficient of VO^{2+}, D_4	3.9×10^{-10} m^2·s^{-1}
Diffusion coefficient of VO_2^+, D_5	3.9×10^{-10} m^2·s^{-1}
Hydrogen diffusion coefficient in electrolyte, D_{H^+}	9.312×10^{-9} m^2·s^{-1}
Conductivity of graphite felt, σ_s	255 S·m^{-1}
Electronic conductivity of bipolar plate, σ_{bp}	1000 S·m^{-1}
Electrolyte viscosity, μ	4.928×10^{-3} Pa·s
Carman-Kozeny constant, K_{CK}	4.28
OCP at reference state, E'_0	1.4 V

$$i_{neg} = aFk_{neg}(c_2^s)^{\alpha_{a,neg}}(c_3^s)^{\alpha_{c,neg}}\left[\exp(\frac{\alpha_{a,neg}\eta_{neg}F}{RT}) - \exp(-\frac{\alpha_{c,neg}\eta_{neg}F}{RT})\right]$$
$$i_{pos} = aFk_{pos}(c_4^s)^{\alpha_{a,pos}}(c_5^s)^{\alpha_{c,pos}}\left[\exp(\frac{\alpha_{a,pos}\eta_{pos}F}{RT}) - \exp(-\frac{\alpha_{c,pos}\eta_{pos}F}{RT})\right] \quad (28)$$

where c_i^s (i = 2, 3, 4, 5) are the concentrations of reaction ions on the fiber surface in porous electrodes. α is transfer coefficient, and a is specific surface area. η denotes the electrochemical reaction overpotential in porous electrode. The electrochemical reaction constant associated with the temperature is expressed by [5]:

$$k_{neg} = k^{ref}_{neg}\exp\left(\frac{FE^{0'}_{neg}}{R}\left(\frac{1}{T^{ref}} - \frac{1}{T}\right)\right)$$
$$k_{pos} = k^{ref}_{pos}\exp\left(\frac{FE^{0'}_{pos}}{R}\left(\frac{1}{T^{ref}} - \frac{1}{T}\right)\right) \quad (29)$$

where k^{ref} is the electrochemical reaction rate at reference temperature. $E^{0'}$ denotes the equilibrium potential at negative and positive sides.

Due to the electrolyte circulation between the cells and reservoirs, the change in SOC at the inlet of electrodes are rather slow. It is appropriate to assume that the mass transfer rates and electrochemical reaction rates on reaction surfaces is in quasi-equilibrium state, which is described by [8]:

$$Fk^{mt}_{neg}(c_2 - c_2^s) = -Fk^{mt}_{neg}(c_3 - c_3^s) = Fk_{neg}(c_2^s)^{\alpha_{a,neg}}(c_3^s)^{\alpha_{c,neg}}\left[\exp(\frac{\alpha_{a,neg}\eta_{neg}F}{RT}) - \exp(-\frac{\alpha_{c,neg}\eta_{neg}F}{RT})\right]$$
$$Fk^{mt}_{pos}(c_4 - c_4^s) = -Fk^{mt}_{pos}(c_5 - c_5^s) = Fk_{pos}(c_4^s)^{\alpha_{a,pos}}(c_5^s)^{\alpha_{c,pos}}\left[\exp(\frac{\alpha_{a,pos}\eta_{pos}F}{RT}) - \exp(-\frac{\alpha_{c,pos}\eta_{pos}F}{RT})\right] \quad (30)$$

Local mass transfer coefficient could be obtained based on the experimental correlation [28]:

$$k^{mt}_{neg} = k^{mt}_{pos} = 1.6 \times 10^{-4}\vec{v}^{0.4} \quad (31)$$

where v denotes the electrolyte velocities in porous electrodes. Overpotentials of electrochemical reactions in porous electrodes are expressed by:

$$\eta_{neg} = \phi_s - \phi_e - E^{0'}_{neg}$$
$$\eta_{pos} = \phi_s - \phi_e - E^{0'}_{pos} \quad (32)$$

With the effect of temperature on the equilibrium potential considered, the equilibrium potentials are described by Nernst equation [8]:

$$E^{0'}_{neg} = E^{0,ref}_{neg} + \frac{dE^0_{neg}}{dT}(T - T^{ref}) + \frac{RT}{F}\ln\left(\frac{c_3}{c_2}\right)$$
$$E^{0'}_{pos} = E^{0,ref}_{pos} + \frac{dE^0_{pos}}{dT}(T - T^{ref}) + \frac{RT}{F}\ln\left(\frac{c_5(c_{H^+}/c^{ref})^2}{c_4}\right) \quad (33)$$

where $\frac{dE^0_j}{dT}(j = neg, pos)$ denotes the temperature derivative of equilibrium potential. $E^{0,ref}_j$ is equilibrium potential at reference state in reference [29], where vanadium ions concentrations of each valance are 1 mol/L, $c^0_{H^+}$ and T^{ref} are concentration of hydrogen ion and operational temperature, which are 3 mol/L and 298 K respectively. $E^{0,ref}_{pos} - E^{0,ref}_{neg}$ can be calculated by open circuit potential E'_0 and hydrogen ion concentration at reference state as:

$$E^{0,ref}_{pos} - E^{0,ref}_{neg} = E'_0 - \frac{RT}{F}\ln(c^0_{H^+}/c^{ref})^2 \quad (34)$$

Thus, the terminal voltage of cell stack can be expressed as:

$$E_{stack} = \sum_n\left[E'_0 - \frac{RT}{F}\ln(c^0_{H^+}/c^{ref})^2 + \frac{dE^0_{pos}}{dT}(T - T^{ref}) + \frac{RT}{F}\ln\left(\frac{c_5(c_{H^+}/c^{ref})^2}{c_4}\right) - \frac{dE^0_{neg}}{dT}(T - T^{ref}) - \frac{RT}{F}\ln\left(\frac{c_3}{c_2}\right) + IR + \eta_{pos} - \eta_{neg} + \phi^D_{pos} - \phi^D_{neg}\right] \quad (35)$$

2.5. Boundary conditions and initial values

At $y = 0$, $x^B_n < x < x^-_n$ and $x^M_n < x < x^+_n$, the inlet velocity and inward currents are solved as described as:

$$-\vec{n}\cdot\vec{v} = \frac{\omega^{ch}_n}{A^{ch}} \quad (36)$$

$$\int_{\partial\Omega} i_e dl = (I^{ch}_n)_{in} \quad (37)$$

At $y = y_L$, $x^B_n < x < x^-_n$ and $x^M_n < x < x^+_n$, the outlet pressure, diffusion flux and inward currents are described as:

$$p = p_{out} \quad (38)$$

$$-\vec{n}\cdot D^{eff}_i \nabla c_i = 0 \quad (39)$$

$$\int_{\partial\Omega} i_e dl = (I^{ch}_n)_{out} \quad (40)$$

Species concentrations at inlets of stack are derived from outflow concentrations and electrolyte velocity as:

$$V_{res}\frac{dc^{in}_i}{dt} = \omega c^{out}_i - \omega c^{in}_i,\ c^{in}_i(t = 0) = c^0_i, \quad (41)$$

where ω denotes the electrolyte flow rate and V_{res} is the electrolyte volume in reservoirs.

At the bottom and top of bipolar plate domains and membrane domains, boundaries are treated to be electrically insulated. At $y = 0$ and $y = y_L$,

$$-\vec{n}\cdot\vec{i}^B = -\vec{n}\cdot\vec{i}^M = 0 \quad (42)$$

At the membrane and electrode interfaces of negative side $x = x^-_n$,

$$c^m_2 = c^{interface}_2,\ c^m_3 = c^{interface}_3,\ c^m_4 = 0,\ c^m_5 = 0, \quad (43)$$

$$-\vec{n}\cdot\vec{N}_{H^+} = -\vec{n}\cdot i_e/F \quad (44)$$

At the membrane and electrode interfaces of positive side $x = x^M_n$,

$$c^m_2 = 0,\ c^m_3 = 0,\ c^m_4 = c^{interface}_4,\ c^m_5 = c^{interface}_5, \quad (45)$$

Table 6
Configurations and operation conditions for model validation.

Parameter	Value in [30]
Ratio of channel length to cross-sectional area, L^{ch}/S^{ch}	$2.13 \times 10^{3}\ m^{-1}$
Ratio of manifold length to cross-sectional area, L^{ma}/S^{ma}	$16.4\ m^{-1}$
Electrode height, L_h	0.26 m
Electrode width, L_w	0.3 m
Electrode thickness, L_d	0.004 m
Electrode porosity, ε	0.93
Electrode specific area, a	$1.62 \times 10^{4}\ m^{-1}$
Carbon fiber diameter, d_{fiber}	1.76×10^{-5} m
Electrolyte volume in each reservoir, V_{res}	30 L
Initial SOC	0.15
Total vanadium concentration, c_{total}	$2000\ mol{\cdot}m^{-3}$
Initial negative H^+ concentration, c^0_{neg,H^+}	$3300\ mol{\cdot}m^{-3}$
Initial positive H^+ concentration, c^0_{pos,H^+}	$5300\ mol{\cdot}m^{-3}$
Ambient temperature, T_a	298 K
Nusselt number, Nu_f	100
Cell number	15

$$-\vec{n}\cdot\vec{N}_{H^+} = \vec{n}\cdot i_e/F \tag{46}$$

At the surfaces of end plates, current densities are applied as:

$$-\vec{n}\cdot i^E = \begin{cases} -i_a, & x = 0 \\ i_a, & x = x_N^E \end{cases} \tag{47}$$

where i_a is applied current density of battery stack.

3. Results and discussion

The governing equations of the mathematical model were solved with COMSOL Multiphysics utilizing the finite element method and the relative error tolerance was set to 10^{-6}. The *Darcy's Law* option was utilized for the simulation of fluid flow in porous electrode. The *Transport of Diluted Species* and *Primary Current Distribution* options were employed for the modeling of mass transport and electrochemical kinetics respectively. Electrolyte flow rates and electrical resistances in flow frame were updated iteratively in the simulation.

3.1. Model validation

The simulation results of battery performance and temperature were compared with investigation results of a kilowatt scale VRFB system from literature. Battery specifications and operation parameters employed in numerical simulations are listed in Table 6.

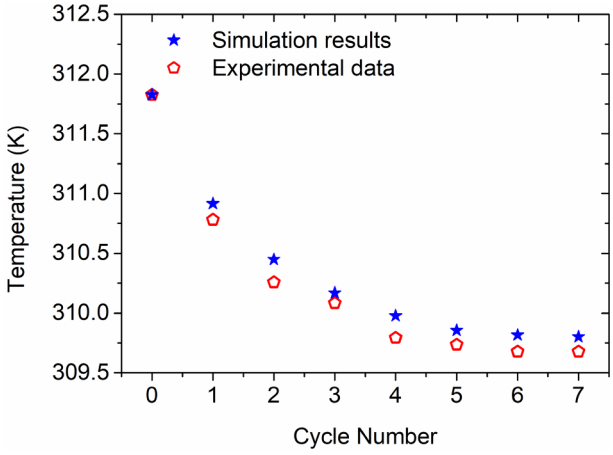

Fig. 3. Comparison of calculated temperature in reservoir with experimental data.

To validate the feasibility and accuracy of this model, the battery performance at different current densities and electrolyte flow rates is demonstrated. Our calculated results show good agreement with the experimental data [30] at different current densities and flow rates as shown in Fig. 2, indicating that our model could accurately capture the charge-discharge performance at ranges of current densities and electrolyte flow rates.

The heat transfer processes in VRFB system composed of stack, reservoirs and pipes was simulated during charge-discharge cycles. As shown in Fig. 3, electrolyte temperature in reservoirs at the end of each cycle was compared with experimental data from Kim et al. [30]. The temperature at the beginning of charge-discharge cycling is 311.8 K at the current density of 80 mA/cm^2 and the ambient temperature is 298 K in Kim's experiments. To validate the accuracy of simulation results, the initial temperature of electrolyte and ambient temperature in simulation are set to be identical with the measured data from Kim's experiments. The calculated temperature of electrolyte in reservoirs after each cycle agrees well with experimental data. Due to the large gap between electrolyte temperature and ambient temperature, the total heat dissipation in VRFB system is larger than heat generation in each cycle. Herein, the temperature drops along with cycling. Gradually, the temperature gap decrease, leading to the reduction of heat dissipation. The temperature drop slows down consistently. The slight discrepancy of temperature is aroused by the deviations of the convection heat transfer

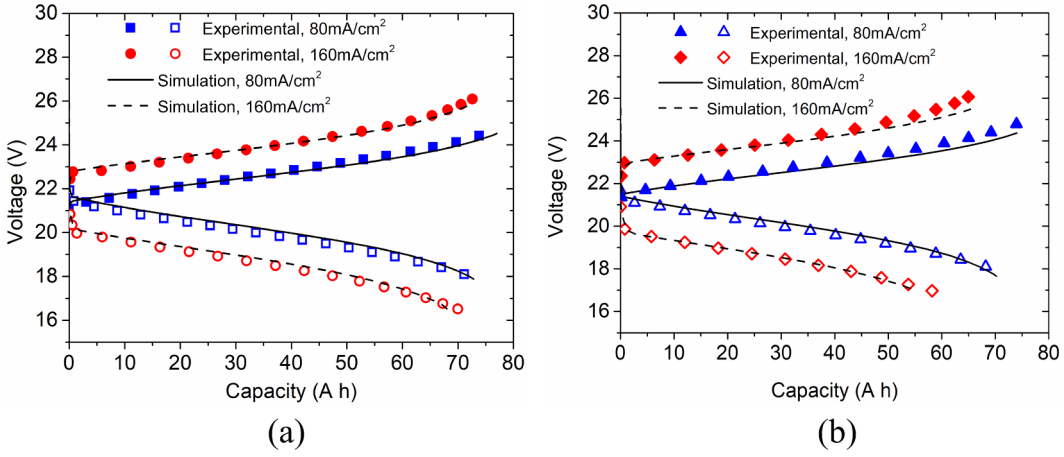

Fig. 2. Comparison of simulation results at (a) 4 L/min and (b) 6 L/min with experimental data in literature.

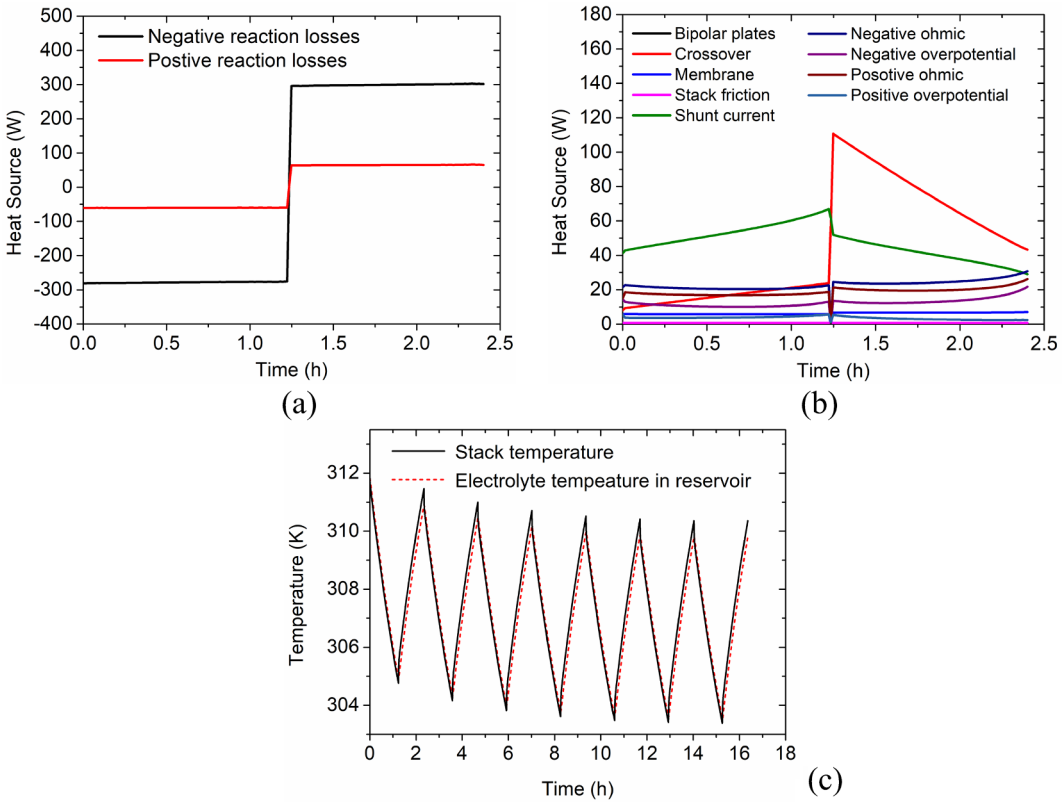

Fig. 4. (a) Reversible, (b) irreversible heat sources in stack and (c) temperature of stack and reservoir electrolyte during operation.

between simulation and experimental conditions at the surfaces of stack and reservoirs.

3.2. Heat sources in cells stack

Fig. 4 shows the heat sources and temperature in the stack at current density of 80 mA/cm^{-2}. Heat sources are mainly located at porous electrodes, and heat dissipation into ambience occurs at the surface of reservoirs and stack. The heat sources are negative at charging stage and positive at discharge stage for both positive and negative electrochemical reactions in the stack. Although reaction heat sources are associated with temperature which fluctuates all the time, the variation range of temperature is rather small and can be negligible during charge-discharge cycles. Thus, heat sources for negative and positive electrochemical reactions stay nearly constant as shown in Fig. 4(a). Reaction heat sources at negative side are nearly 300 W, which is about ten times of that at positive side. During both charge and discharge stages, the reversible heat sources related to electrochemical reactions dominate heat generation, and dramatically influences the temperature in stack and reservoirs.

Other irreversible heat sources in stack are positive and lead to only heat generation. Fig. 4(b) shows that the heat sources related to vanadium ions crossover and shunt currents in flow frame are rather higher than other irreversible heat sources in the stack. The shunt currents are determined by cell voltage, thus, the tendency of heat sources related to shunt currents is consistent with terminal voltage of the stack. Heat sources associated with chemical reactions of vanadium crossover remain rather small during charge stage, while it becomes much larger during discharge stage as shown in Fig. 4(b). There are three transport modes of all the species crossover membranes including diffusion, convection and migration. The vanadium ion diffusion is mainly determined by concentration, which is similar for charge and discharge stages. Thus, the diffusion ion fluxes are nearly the same. The convection fluxes of vanadium ions are also negligible due to the small permanent pressure deviation across the membrane. Due to the opposite direction of current, the migration term largely influences the ion flux, leading to the sharply growth of heat sources for vanadium crossover through membrane from the charge stage to the discharge stage. In the charge period, vanadium concentration of V^{2+} and $VO_2{}^+$ increase gradually. Therefore, the concentration difference across the membrane grows up, leading to the increase in diffusion flux of V^{2+} and $VO_2{}^+$. Herein, the heat sources associated with vanadium crossover increase due to the chemical reaction with V^{3+} and VO^{2+} in electrolyte. Similarly, the decrease of concentration difference for V^{2+} and $VO_2{}^+$ results in the reduction of vanadium flux across membrane, accompanying with the decrease of heat sources consistently. In summary, transition of the current direction shows dominate influence on the heat sources associated with the reactions of vanadium ions across the membranes, while the diffusion of V^{2+} and $VO_2{}^+$ influences the variation trend in charge and discharge stages separately.

During charge stages, stack temperature decreases due to the endothermic characteristics of electrochemical reactions as shown in Fig. 4(c). At the end of charge stages, stack temperature achieves the minimum value among each cycle. After the battery's state is switched to discharge stage, stack temperature grows up sharply with the dominate influence of heat production associated with electrochemical reactions. During the charge-discharge cycling, electrolyte flows cyclically between stack and reservoirs through flow pipes. The electrolyte temperature is determined by the heat convection through forced electrolyte flow and heat dissipation at the surfaces of stack, pipes and reservoirs. Along with the electrolyte flow from stack to the reservoirs, electrolyte temperature varies due to the heat transfer through the surfaces, resulting in the temperature discrepancies of electrolyte in reservoirs compared with the stack temperature. Electrolyte temperature in reservoir tends to be fluctuated regularly after several cycles.

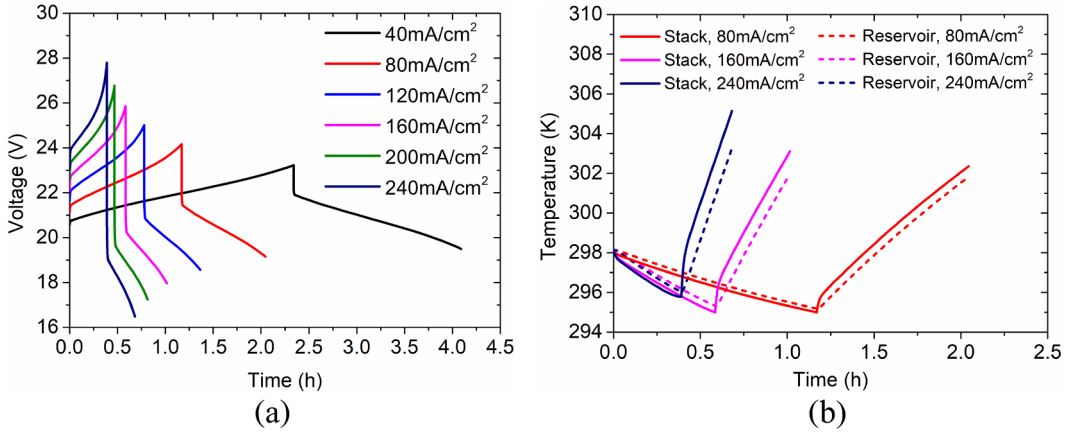

Fig. 5. (a) Terminal voltage, (b) temperature of stack and reservoir electrolyte for different current densities.

3.3. Effect of current densities

Current density plays a key role in determining the battery performance as shown in Fig. 5(a). Due to the endothermic characteristics of electrochemical reactions during charge period, stack temperature at different current densities remains decreasing tendency. This indicates that reversible heat sources associated with electrochemical reactions are larger than irreversible heat sources and heat transport through walls of stack and reservoirs. Resulted from large heat capacity of aqueous electrolyte in VRFB, the heat absorption of electrolyte in stack are efficient when electrolyte flowing through the porous electrodes. The stack temperature decreases gradually along with the battery charging processes as depicted in Fig. 5(b). With an increase in current densities, heat absorption in stack grows up during charge stage, resulting in acceleration of temperature drop. During the discharge period, all the heat sources in stack are positive and stack temperature grows at different current densities. In operation cycle, stack temperature fluctuations are approximately up to 10 K, and electrolyte temperature in reservoirs remained little difference compared with stack temperature.

3.4. Effect of electrolyte flow rate

In the VRFB, circulated electrolyte provides the active substances for electrochemical reactions in porous electrodes, thus flow rate of electrolyte needs to be sufficiently high. Whereas the pressure drop grows up sharply with an increase in electrolyte flow rate, consuming large pump power and decreasing system energy efficiency. Hence, it is of great importance to balance the active substances transport and pump power consumption. Moreover, electrolyte also conducts efficient convection heat transport between stack and reservoirs due to high thermal capacity.

Fig. 6(a) shows that poor mass transport of low flow rate in porous electrodes hinders the electrochemical reactions of vanadium ions conversions. Consequently, terminal voltage of battery stack shows high charging voltage and low discharging voltage, resulting from the large mass transport resistance. Fig. 6(b) shows that heat transfer between stack and reservoir electrolyte becomes quite affordable with the growing up of electrolyte flow rate. As a result, the temperature in battery stack achieves no apparent difference except low flow rate of 2 L/min. Moreover, there is no obvious influence of flow rates for the electrolyte temperature in reservoirs as shown in Fig. 6(c). This is due to the abundant electrolyte with high heat capacity in reservoirs, diminishing the influence of heat transfer through pumped electrolyte flow.

3.5. Effect of nonuniform electrolyte distribution in flow frame

In the VRFB stack, electrolyte is fed into cells through channels and manifolds in flow frame. At the normal state, electrodes specifications such as permeability among different cells keep almost the same. Electrolyte distribution among each cell is uniform as shown in Fig. 7(a) with no blockage. However, at extremely high temperature, precipitation of VO_2^+ in positive electrolyte would change the permeability of porous electrodes. Considering the situation that the middle cell (cell 8) in stack is partially blocked, the flow rate distribution of positive electrolyte among different cells for different blockage ratio are demonstrated as shown in Fig. 7(a). With the increase of blockage ratio, flow rate of positive electrolyte in middle cell decease sharply. Electrolyte is uniformly distributed into the other 14 cells via the connected manifolds and channels in flow frame. The discharge capacity of VRFB for different blockage ratio was calculated with the initial SOC state of 0.85. As shown in Fig. 7(b), discharge capacity reduces by 80% with the blockage ratio of 25%. Compared with unblocked cells in stack, convection mass transport along flow direction is reduced due to the dramatically decrease of flow rate in middle cell. At the end of discharge stage, reactant exhaustion near the outlet of middle cell results in sharp decrease of discharge voltage, which represents the end of discharge stages. The results show that discharge capacity is sensitive to the nonuniformity of electrolyte distribution, and precipitation in positive electrolyte affects the battery performance severely.

4. Conclusions

In this work, a two-dimensional mathematical model for the VRFB stack is reported. The effect of nonuniform electrolyte distributions in the flow frame is considered via a flow network equivalence method. The model is validated via the comparisons of stack performance with measured data in literature. During charge-discharge stages and operation cycles, simulation results such as battery voltage and electrolyte temperature in reservoirs meet the experimental data in literature accurately at different operation conditions. The reversible and irreversible heat sources associated with mass, charge transport and electrochemical reactions are determined and effects of current densities and flow rates on stack performance and temperature are studied. The capacity reduction during discharge stage caused by the vanadium precipitation blockage in stack is also investigated. The results show that stack temperature fluctuations could be up to 10 K at different current densities and flow rates. With the blockage ratio of 25% in positive electrode of middle cell, discharge capacity of VRFB reduces by 80%. Discharge capacity of the VRFB is sensitive to the nonuniformity of electrolyte distribution in partially blocked stack. Furthermore, this

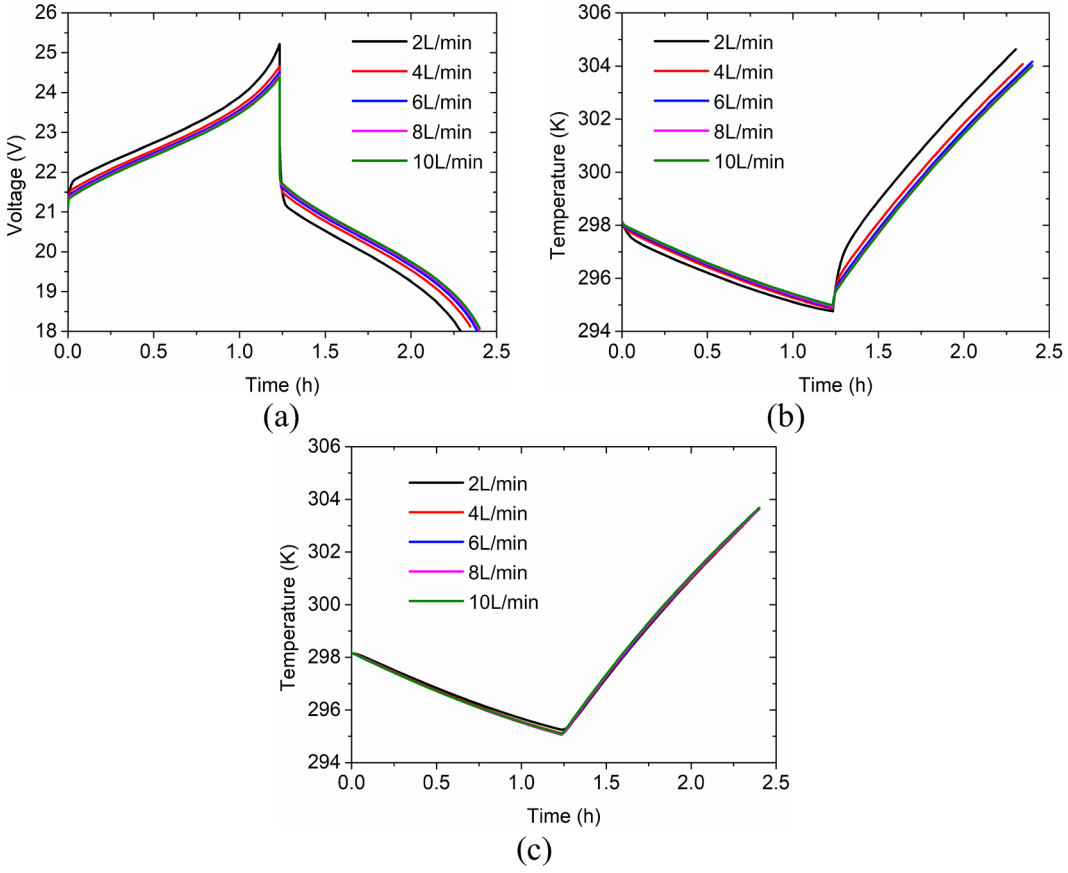

Fig. 6. (a) Battery voltage, (b) stack temperature and (c) electrolyte temperature in reservoirs for different flow rates.

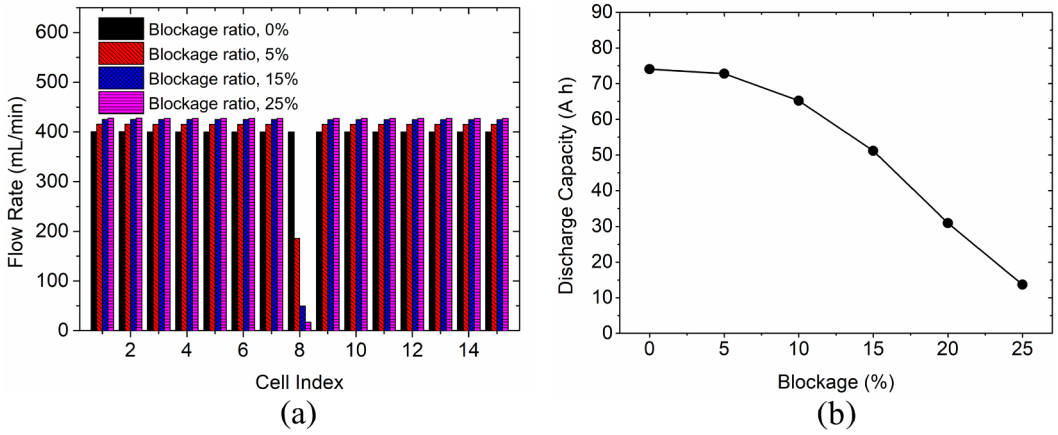

Fig. 7. (a) Flow rate distribution and (b) discharge capacity for different blockage ratio in middle cell (cell 8).

model could be utilized to investigate the transport processes in VRFB system with different flow frame specifications in the future.

Acknowledgments

This work was supported by the Open Projects of State Key Laboratory of Multiphase Flow in Power Engineering of China and a grant from the Research Grant Council of the Hong Kong Special Administrative Region, China (Project No. T23-601/17-R).

Appendix A. Supplementary material

Supplementary data to this article can be found online at https://doi.org/10.1016/j.applthermaleng.2019.02.037.

References

[1] X.L. Zhou, T.S. Zhao, L. An, Y.K. Zeng, L. Wei, Critical transport issues for improving the performance of aqueous redox flow batteries, J. Power Sources 339 (2017) 1–12.
[2] L. Li, S. Kim, W. Wang, M. Vijayakumar, Z. Nie, B. Chen, J. Zhang, G. Xia, J. Hu, G. Graff, J. Liu, Z. Yang, A stable vanadium redox-flow battery with high energy density for large-scale energy storage, Adv. Energy Mater. 1 (2011) 394–400.
[3] M. Li, T. Hikihara, A coupled dynamical model of redox flow battery based on chemical reaction, fluid flow, and electrical circuit, IEICE Trans. Fundam. Electron. Commun. Comput. Sci. E91-A (2008) 1741–1747.
[4] A.A. Shah, M.J. Watt-Smith, F.C. Walsh, A dynamic performance model for redox-flow batteries involving soluble species, Electrochimica Acta 53 (2008) 8087–8100.
[5] H. Al-Fetlawi, A.A. Shah, F.C. Walsh, Non-isothermal modelling of the all-vanadium redox flow battery, Electrochimica Acta 55 (2009) 78–89.
[6] D. You, H. Zhang, J. Chen, A simple model for the vanadium redox battery, Electrochimica Acta 54 (2009) 6827–6836.

[7] K.W. Knehr, E.C. Kumbur, Open circuit voltage of vanadium redox flow batteries: discrepancy between models and experiments, Electrochem. Commun. 13 (2011) 342–345.
[8] K.W. Knehr, E. Agar, C.R. Dennison, A.R. Kalidindi, E.C. Kumbur, A Transient vanadium flow battery model incorporating vanadium crossover and water transport through the membrane, J. Electrochem. Soc. 159 (2012) A1446–A1459.
[9] K. Bromberger, J. Kaunert, T. Smolinka, A model for all-vanadium redox flow batteries: introducing electrode-compression effects on voltage losses and hydraulics, Energy Technol. 2 (2014) 64–76.
[10] Y. Lei, B.W. Zhang, B.F. Bai, T.S. Zhao, A transient electrochemical model incorporating the Donnan effect for all-vanadium redox flow batteries, J. Power Sources 299 (2015) 202–211.
[11] X.-G. Yang, Q. Ye, P. Cheng, T.S. Zhao, Effects of the electric field on ion crossover in vanadium redox flow batteries, Appl. Energy 145 (2015) 306–319.
[12] X.L. Zhou, T.S. Zhao, L. An, Y.K. Zeng, X.H. Yan, A vanadium redox flow battery model incorporating the effect of ion concentrations on ion mobility, Appl. Energy 158 (2015) 157–166.
[13] Y. Lei, B.W. Zhang, Z.H. Zhang, B.F. Bai, T.S. Zhao, An improved model of ion selective adsorption in membrane and its application in vanadium redox flow batteries, Appl. Energy 215 (2018) 591–601.
[14] Z.B. Wei, A. Bhattarai, C.F. Zou, S.J. Meng, T.M. Lim, M. Skyllas-Kazacos, Real-time monitoring of capacity loss for vanadium redox flow battery, J. Power Sources 390 (2018) 261–269.
[15] Z.B. Wei, T.M. Lim, M. Skyllas-Kazacos, N. Wai, K.J. Tseng, Online state of charge and model parameter co-estimation based on a novel multi-timescale estimator for vanadium redox flow battery, Appl. Energy 172 (2016) 169–179.
[16] Z.B. Wei, K.J. Tseng, N. Wai, T.M. Lim, M. Skyllas-Kazacos, Adaptive estimation of state of charge and capacity with online identified battery model for vanadium redox flow battery, J. Power Sources 332 (2016) 389–398.
[17] Q. Xu, T.S. Zhao, P.K. Leung, Numerical investigations of flow field designs for vanadium redox flow batteries, Appl. Energy 105 (2013) 47–56.
[18] Q. Zheng, H. Zhang, F. Xing, X. Ma, X. Li, G. Ning, A three-dimensional model for thermal analysis in a vanadium flow battery, Appl. Energy 113 (2014) 1675–1685.
[19] Y.T. Yan, Y.F. Li, M. Skyllas-Kazacos, J. Sao, Modelling and simulation of thermal behaviour of vanadium redox flow battery, J. Power Sources 322 (2016) 116–128.
[20] S. Konig, M.R. Suriyah, T. Leibfried, A plug flow reactor model of a vanadium redox flow battery considering the conductive current collectors, J. Power Sources 360 (2017) 221–231.
[21] Z.B. Wei, J.Y. Zhao, M. Skyllas-Kazacos, B.Y. Xiong, Dynamic thermal-hydraulic modeling and stack flow pattern analysis for all-vanadium redox flow battery, J. Power Sources 260 (2014) 89–99.
[22] A. Tang, J. Bao, M. Skyllas-Kazacos, Studies on pressure losses and flow rate optimization in vanadium redox flow battery, J. Power Sources 248 (2014) 154–162.
[23] S. König, M.R. Suriyah, T. Leibfried, Model based examination on influence of stack series connection and pipe diameters on efficiency of vanadium redox flow batteries under consideration of shunt currents, J. Power Sources 281 (2015) 272–284.
[24] B.R. Munson, D.F. Young, T.H. Okiishi, Fundamentals of Fluid Mechanics, fifth ed., J. Wiley & Sons, Hoboken, NJ, 2006.
[25] S. Corcuera, M. Skyllas-Kazacos, State-of-charge monitoring and electrolyte rebalancing methods for the vanadium redox flow battery, Eur. Chem. Bull. 1 (2012) 511–519.
[26] C. Sun, J. Chen, H. Zhang, X. Han, Q. Luo, Investigations on transfer of water and vanadium ions across Nafion membrane in an operating vanadium redox flow battery, J. Power Sources 195 (2010) 890–897.
[27] M.M. Tomadakis, T.J. Robertson, Viscous permeability of random fiber structures: comparison of electrical and diffusional estimates with experimental and analytical results, J. Compos. Mater. 39 (2005) 163–188.
[28] D. Schmal, J. Erkel, P.J. Duin, Mass transfer at carbon fibre electrodes, J. Appl. Electrochem. 16 (1986) 422–430.
[29] T. Sukkar, M. Skyllas-Kazacos, Water transfer behaviour across cation exchange membranes in the vanadium redox battery, J. Membr. Sci. 222 (2003) 235–247.
[30] S. Kim, E. Thomsen, G. Xia, Z. Nie, J. Bao, K. Recknagle, W. Wang, V. Viswanathan, Q. Luo, X. Wei, A. Crawford, G. Coffey, G. Maupin, V. Sprenkle, 1 kW/1 kWh advanced vanadium redox flow battery utilizing mixed acid electrolytes, J. Power Sources 237 (2013) 300–309.